A DIGITAL VIDEO MODEL DEFORMATION SYSTEM

A. W. Burner, W. L. Snow, W. K. Goad, B. A. Childers

NASA Langley Research Center
Hampton, Virginia 23665

ABSTRACT

The use of solid-state array cameras and a PC controlled image acquisition system to measure model deformation in a wind tunnel is discussed. This digital system is an improvement to an earlier video model deformation system used at the National Transonic Facility (NTF) which employed high-resolution tube cameras and required the manual measurement of targets on video hardcopy images. The new system eliminates both the vibration-induced distortion associated with tube cameras and the manual readup of video images necessary in the earlier version. Camera calibration and data reduction procedures necessary to convert pixel image plane data from two cameras into wing deflections are presented. Laboratory tests to establish the uncertainty of the new system with the geometry to be used at the NTF are described.

1. INTRODUCTION

The dynamic pressure capability of the National Transonic Facility (NTF) is greater than three times that of other transonic wind tunnels [1] and can cause model wing tip deflections of several centimeters. A number of techniques have been suggested to measure this deflection [2-4]. A photogrammetric approach based on earlier wind tunnel work at NASA Langley with film cameras [5] was chosen for initial measurements because of its inherent rapid data recording of the entire object field. Video cameras were used to acquire data instead of film cameras due to the inaccessibility of cameras which must be housed within the cryogenic, high pressure plenum of this facility [6].

For the tests described in [6] images were recorded with a video hardcopy unit and manually measured with a monocomparator. This manual readup took more than 30 minutes per image pair. The tube cameras used for these initial tests produced acceptable results over a limited range of tunnel conditions provided appropriate corrections were made for electronic and lens distortions [7]. At more severe tunnel conditions additional vibration induced distortion associated with camer tube construction degraded video dat. considerably. To alleviate this vibration-induced distortion associated wit tube cameras and eliminate the manual measurement of video images, a video model deformation (VMD) system using solid-state array cameras and a PC controlled digital video image acquisition system has been developed.

This digital VMD system was not developed for real-time (30 Hz) applications. Real-time systems intended for control purposes require a different philosophy and are not considered here. For continuous flow wind tunnel applications it is usually sufficient to provide rapid data acquisition capability so that deformation data can be acquired at predetermined test points without adversely impacting the data schedule.

2. IMAGE ACQUISITION SYSTEM

An IBM AT personal computer controls two Silicon Video image capture boards [8] ganged to allow simultaneous capture of two 752h x 480v video images in 1/30 s. The video images are digitized into 256 grey levels. A block diagram of the current system is shown in figure 1.

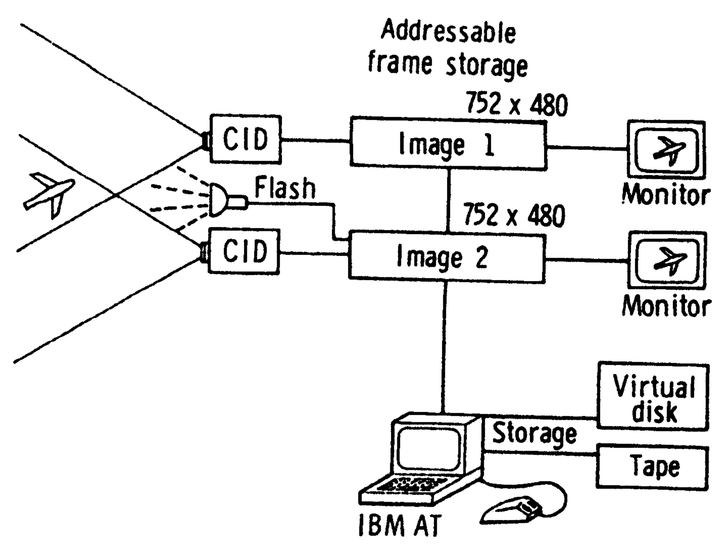

Fig. 1 - Image acquisition system.

Important in the developmental stage is the ability to conveniently interact

with image files and processing algorithms. The current system incorporates the flexibility of a popular operating system (DOS) and higher level programming languages (C, BASIC) to facilitate code development. Software provided for Silicon Video (written in C) allows a PC to digitize, process, display, and store video images. The video images, which are stored as DOS files, can be randomly read with user developed code written in either compiled BASIC or C for such operations as the computation of centroids.

Up to eight consecutive pairs at 1.5 s/pair can be acquired to virtual disk after which the data must be off-loaded at slower rates to a storage medium. A listing of transfer times and storage capacities for several available storage media is presented in Table I.

Medium	Transfer times (s/pair)	Storage capacity (pair)
1.2 MB Diskette	50	1
10 MB Bernoulli cart.	5	13
20 MB Fixed disk	7	27
60 MB Backup tape	9	83

Table I. Media image transfer times and storage capacity.

For cameras such as the GE CID which have 376 pixels horizontally, only half of the horizontal digitizing capability of the image capture boards need be used for a full video image. Then image transfer times would be halved and storage capacity doubled from those listed in Table I. (For tests discussed later the horizontal digitization was kept fixed at 752.) If multiple windows of interest (i.e. only targeted areas of the model) are digitized and stored, transfer rates and storage capacities can be increased significantly. But until the object locations and the experimental conditions are well defined it is best to record full video images as was done for data presented in this report.

3. CAMERA CALIBRATION

The locations of targets on digital images are reported in pixel units. When used for mensuration, however, the mean horizontal and vertical pixel spacings, S_h, S_v in units of mm/pixel must be accurately known. The manufacturer's specification for pixel spacings of solid state video cameras is usually given to 1 or sometimes to 0.1 μmeter. For photogrammetric measurements more accurate values of the horizontal and vertical pixel spacings are needed. For example, a 500 x 500 sensor with an assumed 10 μm pixel spacing will have an error of 25 μm or 2.5 pixels at the edge of field if the pixel spacing is actually 10.1 μm. For this example the pixel spacing must be known to 0.004 μm if an accuracy of 1 μm or 0.1 pixel is desired over the whole sensor.

For photogrammetric applications the critical parameter is the ratio of horizontal-to-vertical pixel spacing rather than the absolute pixel spacing since a change in the apparent camera scale can compensate for sensor scale errors. The nominal vertical pixel spacing and ratio of horizontal-to-vertical pixel spacings serve as the first level of geometrical sensor characterization. The pixel spacing referred to here is that of the camera system which may consist of a sensor and video frame store. (For some interlaced sensors the system vertical pixel spacing will equal 1/2 of the manufacturer's specification.)

The ratio of horizontal-to-vertical pixel spacing can be determined photogrammetrically as part of the resection process by including it as an additional unknown. With proper attention to optical alignment the ratio can also be determined by recording the video image of a known object field and adjusting the ratio of horizontal-to-vertical pixel spacing to correct the scale error in the distorted video image. An alternative to either of the above two approaches is the determination of the ratio with a reticle laid on the sensor. The advantage of using a reticle is that the effects of lenses, distribution of object field points, and alignment are not included in the ratio and a direct measure of system horizontal and vertical absolute pixel spacing is made.

3.1 Use of a Reticle to Determine Pixel Spacing

A suitable reticle pattern for use in determining pixel spacing consists of a 7 x 9 array of equally spaced clear dots (with a diameter greater than several pixels) on an opaque background. For the common 2/3 inch format sensor the reticle would have to be about 6 mm x 8 mm. The reticle can be produced photographically on film or glass plates which have a moderately high resolution and contrast. The locations of the dots on the reticle are then measured with a monocomparator to typically an accuracy of several μm.

The experimental setup consists of a collimated light source (preferably an expanded laser beam) illuminating the reticle which is laid directly on the sensor cover-glass window. The lens and usually the lens mounting plate of the camera must be removed to gain access to the sensor face. The light passing through the reticle will form a shadow image of the 7 x 9 array of dots. The centroids may be computed and fitted in a linear least squares sense to the reticle itself

using the following affine transformation

$$(1) \qquad x' = a_1 + a_2x + a_3y \qquad y' = b_1 + b_2x + b_3y$$

where x',y' are the coordinates of the reticle dots in mm and x,y are the coordinates of the centroided images of the dots in pixel units. The origin for the pixel coordinate system is at the center of the digitized video image with positive x to the right and y upward.

Equation (1) can be rewritten incorporating the mean horizontal and vertical pixel spacings and θ_x, θ_y, the angles between the x' and x axes and between the y' and y axes respectively as

$$(2) \qquad x' = a_1 + (S_h\cos\theta_x)x + (S_y\sin\theta_y)y \qquad y' = b_1 + (-S_h\sin\theta_x)x + (S_y\cos\theta_y)y$$

Figure 2 illustrates this coordinate transformation with a_1 and b_1 set to zero.

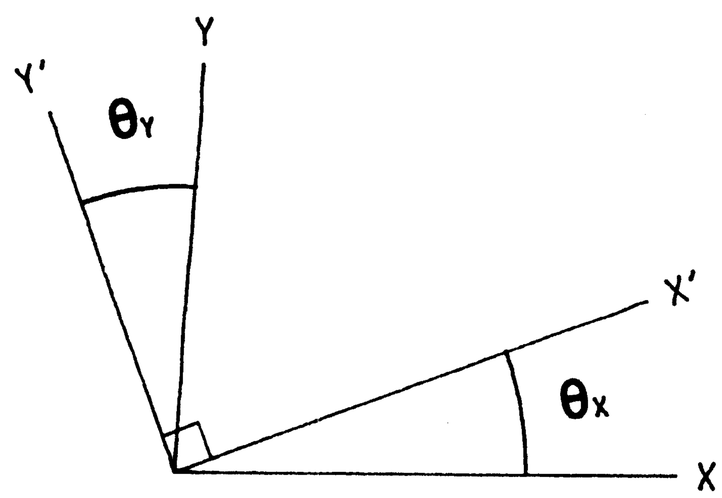

Fig. 2 - Coordinate transformation.

The mean horizontal and vertical pixel spacings are thus related to the affine coefficients by

$$(3) \qquad S_h = (a_2^2 + b_2^2)^{1/2} \qquad S_v = (a_3^2 + b_3^2)^{1/2}$$

The non-perpendicularity, ϕ, of the sensor axes is given by

$$(4) \qquad \phi = \theta_y - \theta_x$$

where

$$(5) \qquad \theta_x = \tan^{-1}(-b_2/a_2) \qquad \theta_y = \tan^{-1}(a_3/b_3)$$

When correcting an arbitrary image it is convenient to set a_1 and b_1 to zero and use the sensor horizontal axis as the reference axis ($\theta_x = 0$; $\theta_y = \phi$). The transformation from pixel units to actual length (mm) on the sensor face expressed in terms of the sensor para meters is then given by

$$(6) \qquad x' = S_hx + S_vy\sin\phi \qquad y' = S_vy\cos\phi$$

which for most applications can be approximated by

$$(7) \qquad x' = S_hx + S_vy\phi \qquad y' = S_vy$$

3.2 Sources of Error in reticle measurement

The location of the targets on the reticle can be measured with a monocomparator to 2 μmeter or less. The introduction of random error into the known reticle measurements indicates that an uncertainty of 2 μm in the comparator measurement (or a centroiding error of 0.2 pixel) for a 7 x 9 array reticle will produce pixel spacing errors less than 0.002 μm for a 500 x 500 sensor with a 10 μm nominal pixel spacing. The corresponding ratio of horizontal-to-vertical pixel spacing will be in error by less than 0.03 % and the angle ϕ will be in error by less than 0.007°.

The reticle will be displaced about 1 mm from the surface of the sensor due to the cover-glass which protects many sensors. This cover-glass may not be parallel to the sensor surface. (A range of 0.1° to 0.3° for the deviation from parallelism has been found for four sensors.) The error due to the reticle not being parallel to the sensor surface can be made negligible by causing the unexpanded He-Ne laser beam to bisect the reflected beams from the cover-glass and sensor. The reflected beam from the cover-glass can often be identified by the interference fringes in the beam caused by reflections from the first and second surfaces of the cover-glass. The dimmer reflected beam from the sensor will usually be the beam nearest to the cover-glass beam.

The collimation of the expanded He-Ne laser light source can be checked with a shearing plate interferometer [9] to ensure that any errors introduced by lack of collimation for the displaced reticle are negligible compared to other errors that are present. Errors due to film curling can be reduced to negligible levels by placing a small glass window on the reticle to flatten it (or by recording the reticle on a glass photographic plate).

Uncompensated temperature and humidity induced scale changes in the reticle can result in erroneous S_h and S_v determinations, but the S_h/S_v ratio critical to photogrammetry applications is unaffected. For the example of a 500 x 500 sensor with a pixel spacing of 10 μmeter and a reticle made on an Estar base film, a reticle temperature rise of 20°C would cause an error in the absolute pixel spacings of 0.004 μm. (The temperature rise of the cover-glasses of several sensors has been found to be about 20°C after warm-up.) A

change in relative humidity of 10% would cause an error of 0.002 μm. If the temperature and relative humidity are monitored and corrections applied, the uncertainty in the absolute pixel spacings due to temperature and relative humidity can be less than 0.001 μm for the above example. Note that whereas temperature equalization for an Estar base film occurs in minutes, humidity effects may take hours to occur.

3.3 Example of Calibrations Made with a Reticle

A reticle photographically produced on Kodak LPF4 film has been used to characterize two CID and two CCD cameras. The reticle consisted of a 7 x 9 array of clear dots with 50 μm diameter on an opaque background. The reticle was measured 6 times with a monocomparator which had a resolution of one μm. The average rms deviation from the mean for the 63 dots was 1.4 μm in x and y.

The centroids of the dots in the video image were determined after subtracting the background grey level. The technique described in 3.1 was used to determine the system mean horizontal and vertical pixel spacings and angle of non-perpendicularity. Results for four cameras are presented in Table II. The rms of the residuals (less than 1.5 μm) when comparing the transformed video images to the reticle was comparable to the comparator error in measuring the reticle.

	S_h (μm)	S_v (μm)	ϕ (deg)
CID1	11.667	13.766	0.08
CID2	11.666	13.767	0.09
CCD1	9.661	9.300	0.01
CCD2	9.658	9.299	0.00

Table II. Sensor Parameters Measured with a Reticle.

The manufacturer's specification of sensor horizontal and vertical pixel spacings for the CID cameras were 23.3 and 13.6 μm. The horizontal and vertical specifications for the CCD cameras were 9.9 and 9.3 μm (1/2 the specified vertical value due to interlace).

To assess the measurement repeatability in determining the system parameters, eight measurements were made on a single camera over a period of 11 days. The reticle was placed in a slightly different location on the sensor surface for each of the measurements. The rms deviations for the eight measurements were 0.0010 μm for the horizontal pixel spacing, 0.0014 μm for the vertical pixel spacing, and 0.010° for the angle of non-perpendicularity.

The reticle is also useful for establishing the repeatability of the centroid operation for the system. For example, for two video images of the reticle acquired 1/30 second apart with a CID camera the rms centroid repeatabilities were 0.015 pixel in x and 0.011 pixel in y. The rms repeatabilities for two video images of the reticle taken four days apart were 0.064 pixel in x and 0.046 pixel in y. For these repeatability checks the locations of the dots on the reticle do not have to be known. The reticle is used simply to produce a very stable video image with well-defined targets.

3.4 LENS CALIBRATION

The lens used to image a scene onto the sensor introduces additional bias error which may be reduced by calibration. The amount of this error depends on the particular lens selected and sensor resolution. For example, the addition of lens distortion parameters into the photogrammetric solution did not generally improve the results for a 9 mm focal length lens used with a low resolution 128 x 128 sensor [10], whereas lens distortion corrections for a 50 mm lens used with a high-resolution tube camera improved the results in [7] by a factor of 2. In [11] a new distortion function was formulated which resulted in an improvement of about 30 % in accuracy for a 12.5 to 75 mm focal length zoom lens used with a 320h x 244v sensor.

The most important parameters to be determined in a lens calibration are the location of the photogrammetric principal point, x_p, y_p, the location of the optical axis intersection with the sensor, x_o, y_o, and the third order radial lens distortion, σ. In relatively low accuracy photogrammetric measurements currently possible with video cameras (compared to large format film cameras [12]), errors introduced by setting x_p, y_p and x_o, y_o to zero can be negligible. Even so, it may still be useful to determine these parameters, or at least establish limits within which these parameters lie, to use when mathematically modeling the measurement.

The photogrammetric principal point, which is the foot of the perpendicular from the perspective center of the lens to the sensor surface, can be found by aligning a low power laser beam (figure 3) to be perpendicular to the sensor active area (with lens removed).

With the lens mounted to the camera and approximately focused on infinity the centroid of the focused laser beam on the video image locates the principal point. The laser beam need not pass exactly through the front nodal point of the lens since for a reasonably corrected lens all parallel rays approximately intersect at the focal plane. In figure 3 the front and rear nodal points coincide to form a

single perspective center for the simplified thin lens model used to illustrate the technique of locating x_p, y_p.

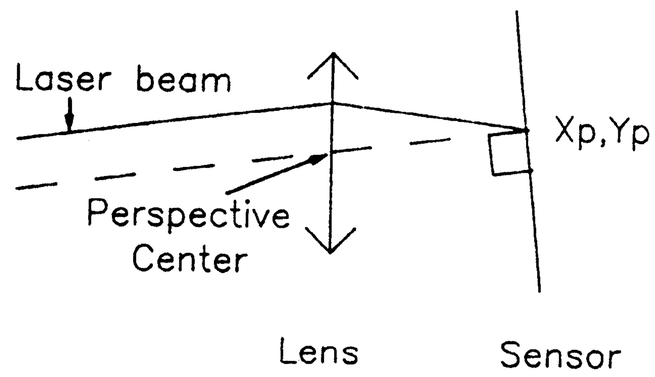

Fig. 3 - Locating x_p, y_p.

Neutral density filters which are used to reduce the laser power density for these measurements should have very little wedge (less than .01° total) so that the angle of the laser beam will not be changed appreciably when the filters are inserted in the beam after alignment. Variable density beamsplitters commonly used for holography have little wedge and have been found to be convenient for reducing the power density of the laser beam.

The intersection of the optical axis and sensor can be found by aligning a low power laser beam to be parallel with the optical axis of the lens mounted on the camera. Since the optical and mechanical axes of commercial grade lenses are typically [13] equal to within 0.05° to 0.2°, an unwedged mirror can be placed either on the camera lens mount (with lens removed) or against the outer lens barrel (perpendicular to the mechanical axis of the lens) and the laser beam aligned to be perpendicular to the mirror. The centroid of the focused laser spot formed by the lens mounted on the camera then locates the approximate intersection of the optical axis with the sensor (fig. 4).

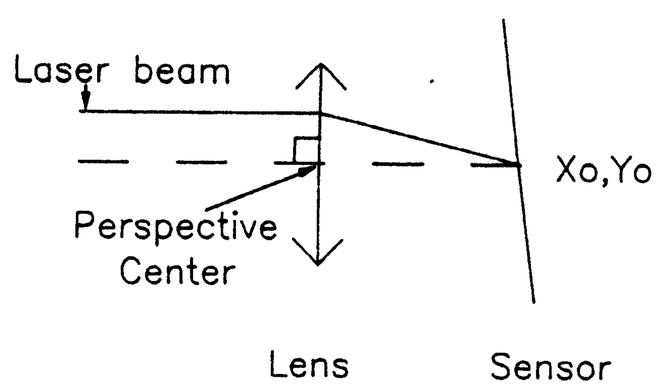

Fig. 4 - Locating x_o, y_o.

The third order radial distortion can be found by imaging a set of known object points located in a plane which is parallel to the sensor. A back-lit metal plate with a 7 x 9 array of 1/8 in diameter holes equally spaced by 2 inches was used to determine the distortion of several CCTV lenses. The locations of the targets in the plane of the plate were known to 1 mil (0.001 inch). The centroided targets of the digitized video image of the back-lit plate were transformed from pixel units to mm using equation (6) and correction parameters found in an earlier sensor calibration. The central 9 points of the back-lit plate were used to determine by linear least squares the conformal transformation coefficients necessary to transform from object plane to image plane. The transformation coefficients found using the central 9 points were then used to transform all 63 plate targets. The radial distortion σ is found from a least squares solution of

$$\delta r = \sigma r^3 \tag{7}$$

where $r = (x'^2 + y'^2)^{1/2}$ is the radial distance from the nominal center of the sensor and δr is the residual vector length for each of the 63 points after transformation.

δr is taken to be negative if the distortion vector points inward toward the center of the sensor and positive if it points outward. A negative σ indicates barrel distortion (typical for a number of CCTV lenses tested) and a positive σ indicates pincushion distortion. For initial determinations of σ it is usually acceptable to set x_o, y_o to zero and to ignore the small radial distortion present in the central 9 points. An example of lens distortion residuals for a 25 mm focal length CCTV lens is presented in figure 5.

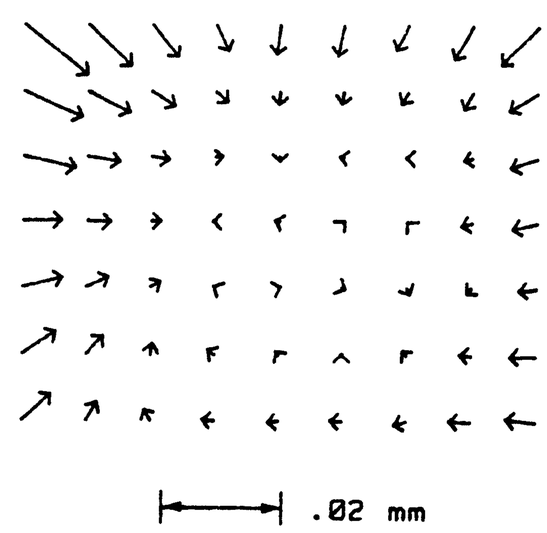

Fig. 5 - Lens distortion for a 25 mm focal length lens

Examples of lens calibration data for 2 CID cameras with 25 mm focal length lenses are presented in Table III. (For similar measurements made on 2 CCD cameras with the same lenses the photogrammetric principal points and optical axis intersections were as much as 0.5 mm from the nominal center of the sensor.) The repeatability of x_p, y_p and x_o, y_o

measurements is typically 0.02 mm. A typical standard deviation for the σ measurements is 0.1×10^{-4} mm^{-2}.

	x_p	y_p	x_o	y_o	σ
	mm		mm		mm^{-2}
CID1	0.09	0.08	0.25	0.01	-1.9×10^{-4}
CID2	-0.01	0.07	0.05	-0.03	-1.3×10^{-4}

Table III. Lens calibration data.

4. PROCEDURE AND DATA REDUCTION

The general procedure for obtaining deflection measurements from video images is described in [6]. For the digital VMD system the manual measurement of hardcopy prints with a monocomparator in [6] is replaced with the computation of centroids on the digital video images. To accurately compute centroids it is necessary to remove background grey level by processing the image so that a background grey level of zero surrounds the targets of interest. The Silicon Video [8] image and local grey level displays are used to examine targets to determine the minimum and maximum grey levels, G_{min}, G_{max} to be mapped into a 0 to 255 grey level range. The new grey levels G_{new} are computed with the Silicon Video software by the following equation

$$(8) \qquad G_{new} = 255(G_{old}-G_{min})/(G_{max}-G_{min})$$

(If this operation is accomplished with user developed code the multiplication by 255 need not be carried out since the centroid computation causes grey levels to be ratioed.) After application of equation (8) the processed image is stored to virtual disk to speed up the centroid computation since the computation requires the digital file be read numerous times.

The effects of several image processing algorithms on two video images of a wing are presented in Table IV. The x',

	CID1		CID2		Triangulation		
	x'	y'	x'	y'	X	Y	Z
Proc.	(μm)		(μm)			(mil)	
None	2.8	4.1	2.6	3.8	7.1	22.2	15.8
Binar	2.2	1.7	1.9	1.7	5.3	16.0	9.5
Thres	1.4	1.2	1.5	1.4	3.4	11.5	6.7
Eq(8)	1.1	0.9	1.1	0.9	3.1	7.5	4.1

Table IV. Effects of image processing.

y' values are rms image plane residuals found from resection on 55 targets whose locations are known to better than 1 mil. The X, Y, Z values are rms object plane residuals found by triangulation (intersection) on the same video pair. For the row labeled "Binar" grey levels are set to zero below G_{min} and to one above. For the row labeled "Thres" grey levels below G_{min} are set to zero and those higher are left unchanged. The application of equation (8) yields an improvement by a factor of 3.1.

The approximate target locations in pixel units necessary to begin the centroid operation are found by either manual settings with a video cursor to form a pixel coordinate file or by use of an old centroid file which contains pixel coordinates of targets with the same numbering scheme and approximate locations as the current image. The target locations of the old centroid file are overlaid on the current image as small boxes centered on the old target locations whose size represents the current centroiding window. Two video images and their corresponding enhanced images with centroid files overlaid are shown in figures 6 and 7.

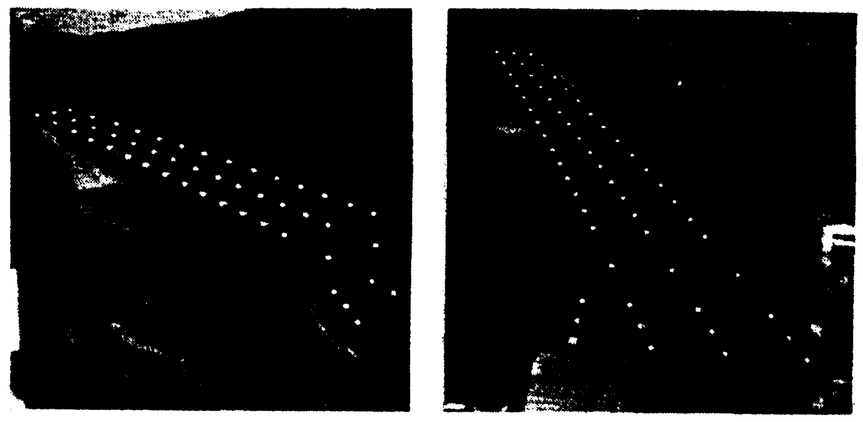

Fig. 6 - Unprocessed images.

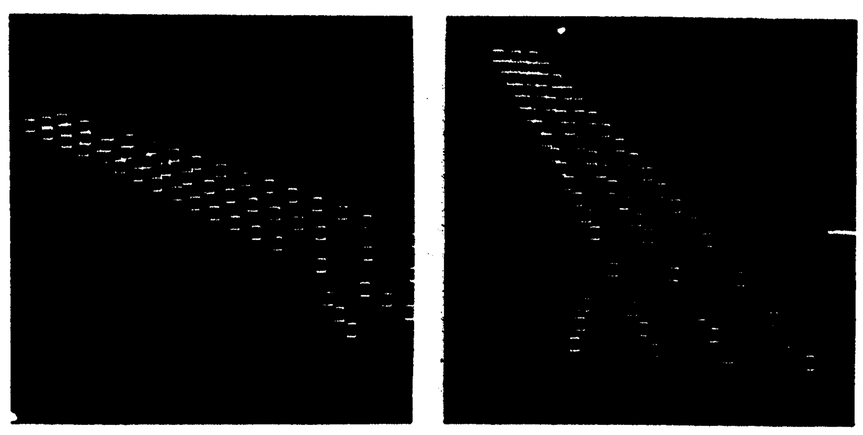

Fig. 7 - Processed images with centroid files overlaid.

The pixel locations, x_t, y_t of targets in an old centroid file which are displaced or distorted somewhat from the current targets can sometimes be transformed to coincide more closely to the new targets, x, y with the following transformation

$$(9) \qquad x = a_1 + a_2x_t + a_3y_t + a_4x_ty_t$$
$$y = b_1 + b_2x_t + b_3y_t + b_4x_ty_t$$

Four current target locations which are determined manually with the video cursor and four old target locations yield a solution for the transformation coefficients.

The pixel coordinates, x, y of the targets on the current image are found with the following centroid relations

(10) $$x = 1/M \sum_i \sum_j jG(i,j)$$

(11) $$y = 1/M \sum_i \sum_j iG(i,j)$$

(12) $$M = \sum_i \sum_j G(i,j)$$

where G(i,j) is the grey level at pixel coordinates (i,j). A typical window size is 13 x 13. Targets generally cover a 5 x 5 array of pixels.

The newly computed centroid file is overlaid on the current image to visually verify that the targets are centered. The image is then centroided a second time using the newly computed centroid file for window locations. The two newly created centroid files are compared to ensure that the centroid operation is not affected by the target window location as can happen if the grey levels surrounding the targets are not zero.

The target numbers, arranged spatially as would be seen on the video image, can be displayed on the computer screen to ensure that targets on the wing are properly numbered and matched to corresponding targets on the second image of the pair. The maximum grey level within each target window can also be displayed to check for variations in irradiance across the field of view or poorly illuminated targets. The array of grey levels within each target window can be displayed along with the minimum, maximum and mean grey values for more detailed examination of questionable targets.

Once the centroid operation is completed for the image pair, the centroids in pixel units are converted to corrected image plane values in mm units with equation (6). These values are then corrected for third order radial lens distortion and x_p, y_p subtracted to yield the corrected centroid coordinates, x_c, y_c

[13] $$x_c = x' - \sigma r^2(x' - x_o) - x_p$$
$$y_c = y' - \sigma r^2(y' - y_o) - y_p$$

where $r^2 = (x' - x_o)^2 + (y' - y_o)^2$. The additional corrections necessary for low temperature, high pressure tunnel conditions as well as the use of the photogrammetric collinearity equations for resection and triangulation to yield three dimensional object plane coordinates are outlined in [6].

In addition to computer codes for the above operations, code has been written to average multiple centroid files, perform three dimensional coordinate transformations of object points, solve the collinearity equations with linear and nonlinear least squares routines for resection and triangulation, plot wing deflection and twist, and transfer data files and programs to and from an HP 9845B desktop computer to make use of some of the routines developed in [6].

5. TEST RESULTS AND DISCUSSION

Tests were conducted at the NTF to establish the best case accuracy of the digital VMD system. These tests were conducted without flow in order to avoid operational constraints and flow effect uncertainties as well as to allow independent verification of measurements. The test wing consisted of a 0.2 inch thick aluminum plate with the planform of a representative transport configuration called Pathfinder I which was used for initial checkout tests at the NTF [6]. The semi-span of the test wing was 26.5 inches. The supporting stand for the test wing was clamped to a vertical traversing table and the wing positioned at the nominal model position. Deflections were produced by forcing the wing tip upwards approximately 0.2 inch with a jack stand. Earlier lab tests had established that a single dial gauge placed at a reference position near the wing tip was sufficient to characterize the deflection for the 57 targets on the wing to about 2 mil.

Two CID cameras with 25 mm focal length lenses mounted in the test section sidewall looked through 1 inch thick fused silica windows at the test wing (fig. 8).

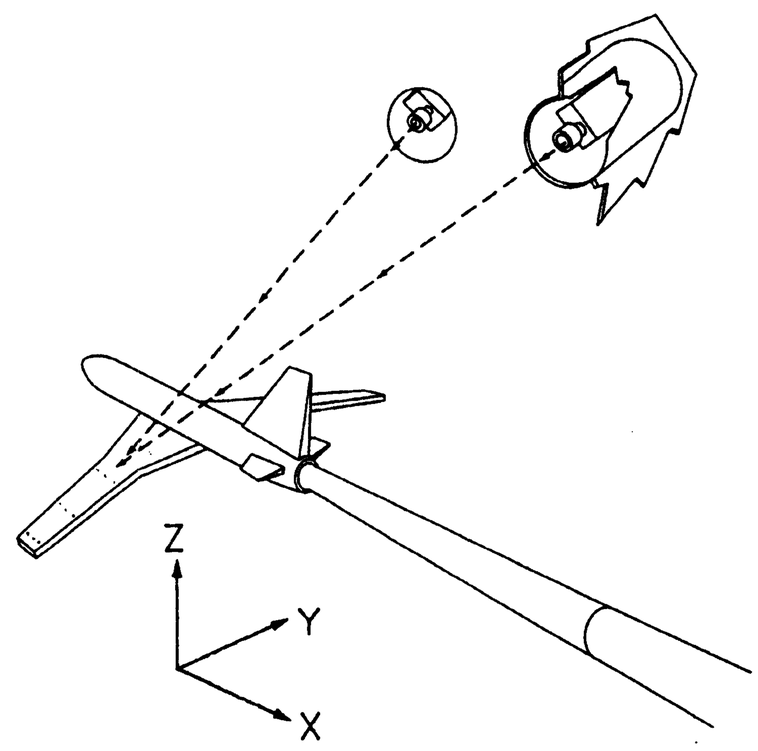

Fig. 8 - Experimental configuration.

The cameras were separated 36 inches. The distance from the cameras to the center of the wing was about 72 inches. Deflection data were taken for two cases, 0° AOA (angle of attack) and 4.3° AOA. The undeflected wing at 0° AOA was used to determine the locations and pointing angles of the two cameras in the tunnel coordinate system by space resection with the collinearity equations [6].

Spanwise deflection data obtained for the 0° AOA case are presented in figure 9 for the 0.5 normalized chord position. Similar plots were obtained for the 0.1 and 0.9 normalized chord positions. The solid line in the plot is a least squares fit to the dial gauge measurements using 2nd and 3rd order terms which characterize the deflection of a clamped beam.

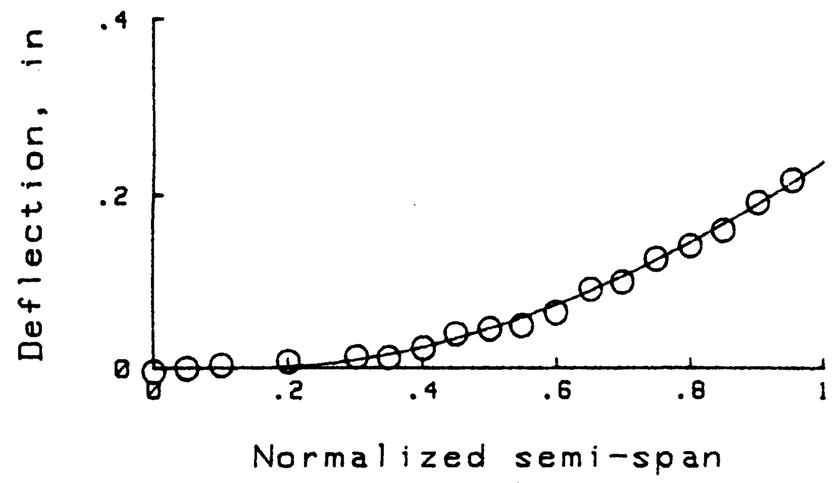

Fig. 9 - Deflection plot at 0° AOA.

Presented in figure 10 are the corresponding residuals from the dial gauge measurements. The rms of the residuals for 55 points was 4.3 mil. The deflection plot in figure 9 was obtained by subtracting the Z values of the undeflected wing from the Z values found for the deflected wing by triangulation. The shift of a deflected target in the Y (spanwise) direction was ignored. This is justified since the shift in the Y direction for a tip deflection of 0.2 inch is less than 1.3 mil. The difference in deflection of 2 points near the tip separated by 1.3 mil in the Y direction is less than 0.03 mil.

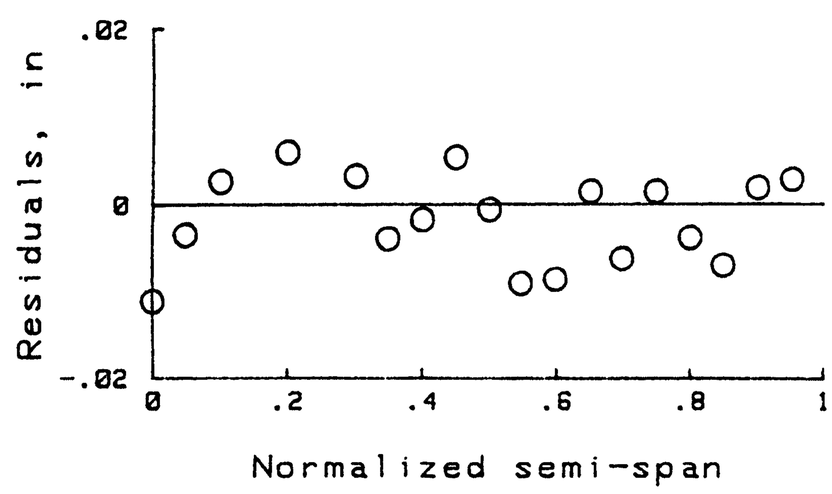

Fig. 10 - Deflection residuals for figure 9.

Wing twist data for the 0° AOA case are presented in figure 11. The twist was computed by taking the vertical difference in deflection from the fore and aft targets along the semi-span and dividing by their separation in the X direction. The dashed curves in figure 11 were obtained with a similar calculation from the dial gauge measurements. For the top curve 3 mil was added to the difference of the dial gauge measurements before computing the twist angle. For the bottom curve 3 mil was subtracted. The separation of the dashed lines points out the high accuracy required in the deflection measurement to provide accurate twist values. The rms residuals from the dial gauge measurements was 0.1° with a maximum error of 0.29°. The solid line in figure 11 is due to least squares fits of the deflection data using second and third order terms. A maximum disagreement of 0.17° occurs at the tip.

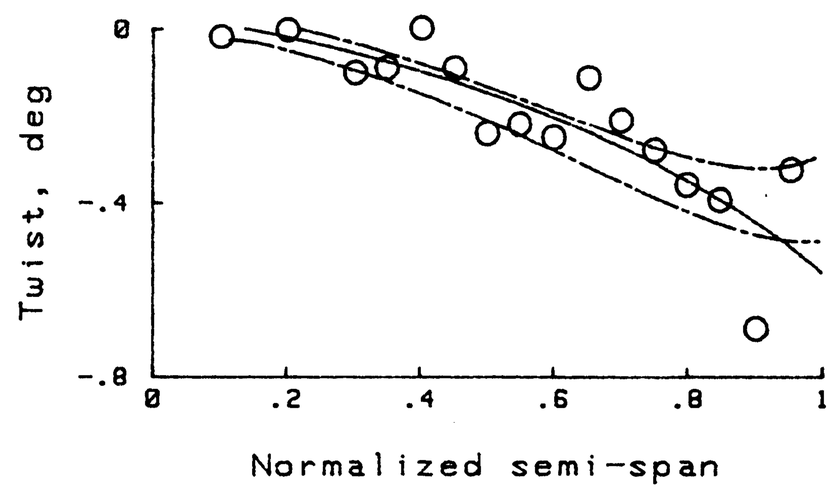

Fig. 11 - Wing twist at 0° AOA.

The 4.3° AOA case was used to simulate the more common occurrence at the NTF in which the model experiences some rigid body motion as well as wing deflection. For these occurrences sensors in the model can be used to provide pitch and roll angles as input to coordinate transformation routines. Translation shifts, predominantly in the X (flow) and Z (upward) directions, are found with a least squares coordinate transformation using inboard undeflected targets. Figure 12 presents

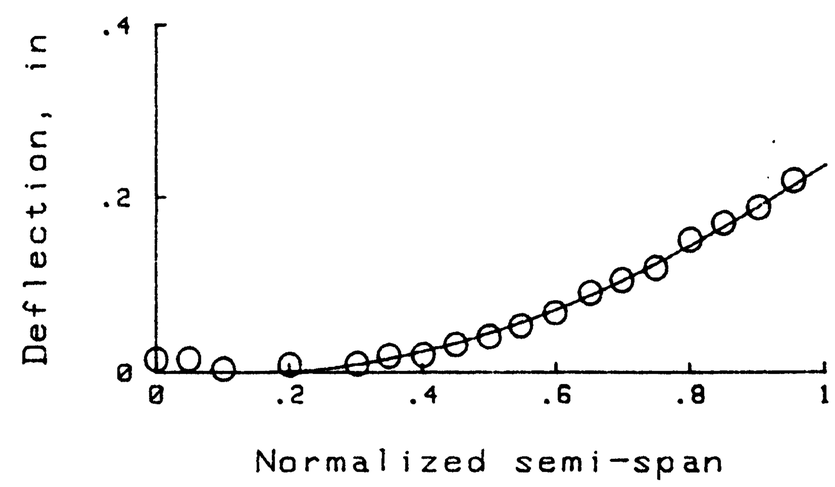

Fig. 12 - Deflection at 4.3° AOA with accurate values of pitch and roll.

deflection data obtained after transforming the deflected data file using transformation coefficients obtained from fitting 55 target locations on the undeflected wing at 4.3° AOA to the undeflected wing at 0° AOA. This data

simulates the case where accurate values of pitch and roll are available. The rms of the residuals of 55 targets was 4.9 mil (figure 13).

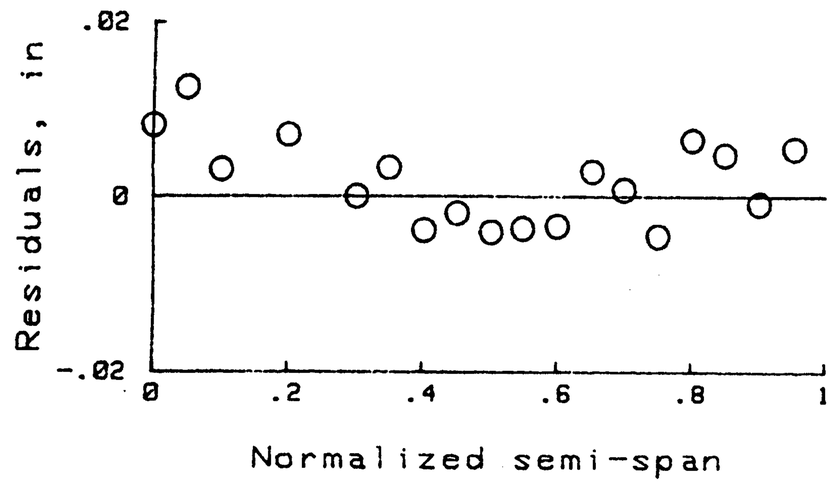

Fig. 13 - Deflection residuals for fig. 12.

Wing twist data for the 4.3° AOA case are presented in figure 14. The rms of the residuals from the dial gauge measurements was 0.17° with a maximum deviation of 0.5°. The dashed curves represent the spread in twist angle due to plus or minus 3 mil in the computation of twist angle from the dial gauge measurements. The solid line which was obtained from least squares fits to the deflection data has a maximum deviation of 0.03° from the dial gauge measurements.

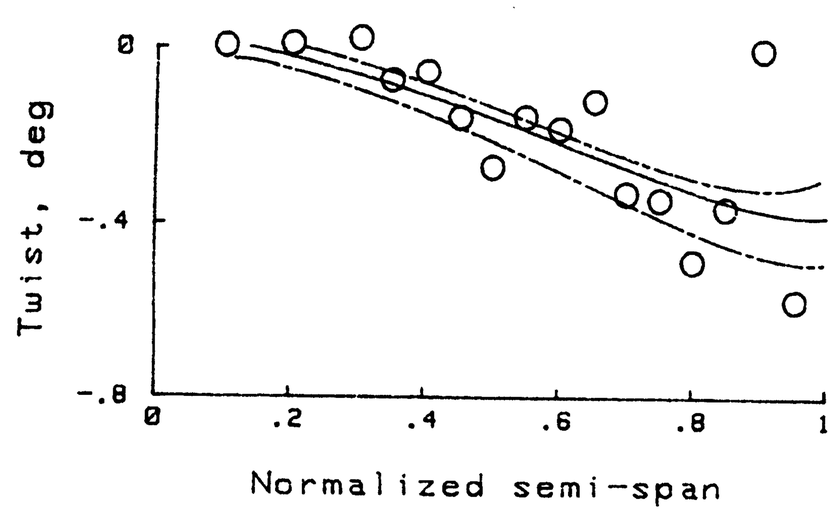

Fig. 14 - Wing twist at 4.3° AOA with accurate values of pitch and roll.

If accurate values for pitch and roll are not available then inboard targets whose deflection is minimal are used to compute them. (Usually the deflected model with wind-on experiences rigid body translation and rotation due to sting bending so that it is not appropriate to use the undeflected model with wind-off to determine pitch, etc. of the model with wind-on.) The 10 inboard targets on the deflected test wing at 4.3° AOA were fitted to the known target coordinates at 0° AOA. The pitch and roll angles found (as well as yaw and three translations) were used to transform the deflected data.

The deflection and wing twist data are presented in figures 15, 16 and 17. Note the change in scale of figure 16 compared to figures 10 and 13.

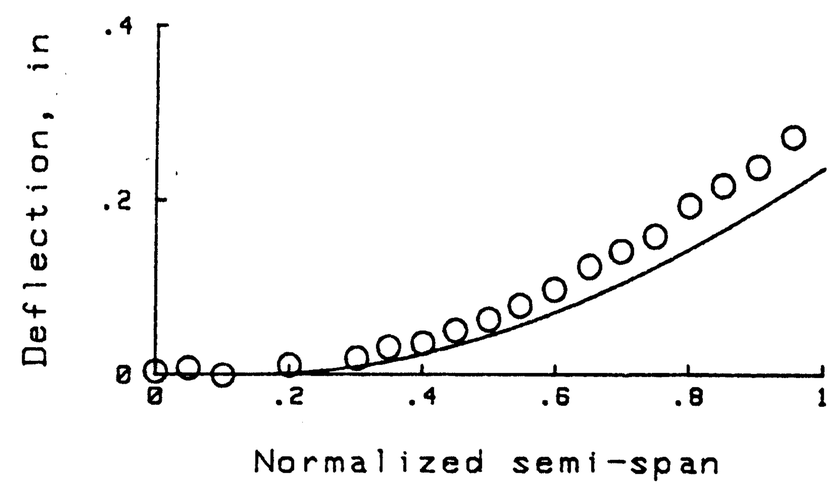

Fig. 15 - Deflection data at 4.3° AOA with pitch and roll determined from 10 inboard targets.

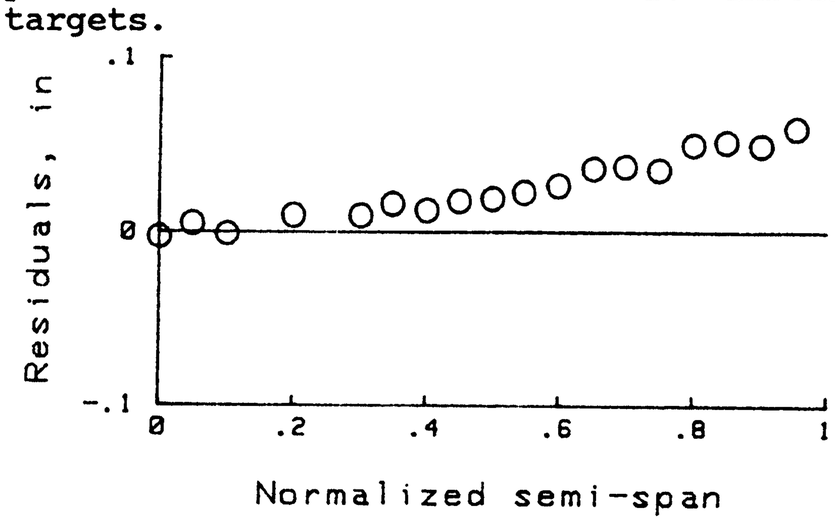

Fig. 16 - Deflection residuals for fig. 15

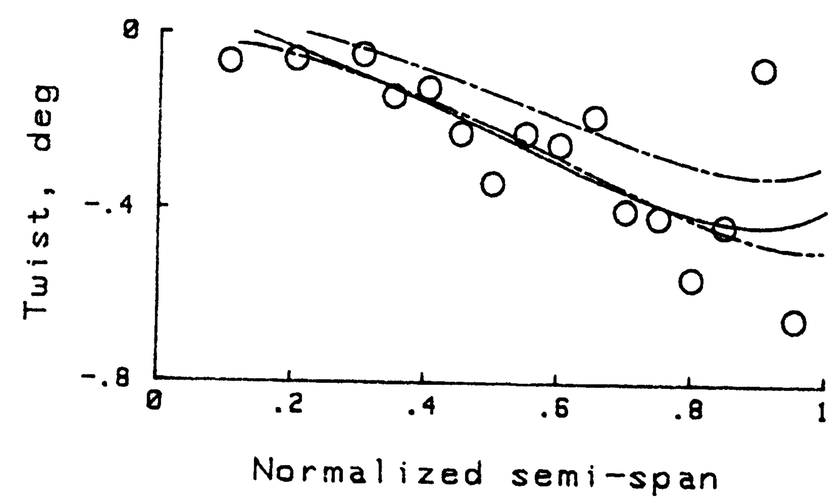

Fig. 17 - Wing twist at 4.3° AOA with pitch and roll determined from 10 inboard targets.

Note that whereas the deflection has a large spanwise-varying bias error ($\simeq$ 60 mil at the tip), the twist plot of figure 17 varies only slightly from that of figure 14. Deflection measurements are highly dependent on roll angle since the deflection error at the wing tip is equal to the product of the semi-span and the sine of the roll error. The roll angle computed using only the 10 inboard targets differed from the correct value by 0.10°

which accounts for 46 mil wing tip deflection error. The deflection error due to pitch error depends on the location of the center of rotation along the X axis. The pitch angle computed using the 10 inboard points differed from the correct value by 0.07° which accounts for an additional 18 mil deflection error near the tip.

The twist angle is independent of roll angle error but directly proportional to the error in pitch. Figure 17 is biased 0.07° less than figure 14 due to the difference in the pitch angles used for the two plots. The rms of the residuals from the dial gauge measurements was 0.13° with a maximum deviation of 0.32°. The maximum deviation for the least squares fit solid line was 0.08°.

Eight video pairs were recorded of the undeflected wing to see if averaging multiple video images (repeats) could reduce the scatter in the deflection residuals. Since with the present software it is more convenient to average centroids rather than to average grey scale and then compute centroids, a comparison of the two approaches was made. The means of the centroids of the eight pairs agreed within 0.007 pixel to the centroids computed after averaging grey scale. Thus if the use of multiple images is shown to be warranted it is sufficient to average centroids rather than average the grey scale and then compute centroids.

The rms deviations from the mean for repeat shots are a measure of the short term repeatability of the system. For camera 1 the rms centroid repeatabilities for 57 targets were 0.030 pixel in x and 0.008 pixel in y. For camera 2 the rms repeatabilities for 55 targets were 0.039 pixel in x and 0.011 pixel in y. For an approximate image-to-object scale of 72, a 0.01 pixel variation in the y direction on the sensor would correspond to a spread of only 0.35 mil in Z (vertical) of the object field. Thus it is not expected that much improvement would occur by using multiple images in the current setup. Deflection and twist plots for a single image pair and for the means of the eight pairs are almost identical and the rms deviations in Z are equal to within 0.5 mil.

As a final example of the capability of the system, data was taken in the lab with camera 1 only to demonstrate the accuracy of the system for controlled single point deflection measurements. Pixels in the vertical direction of the camera were scaled by recording two images of a single target near the wing tip displaced a known distance of 200 mil. The wing was then deflected to 50, 100, and 150 mil (as measured with a dial gauge) and images acquired, centroided and scaled to yield interpolated values at the three locations. For tests with 25, 75 and 200 mm lenses the maximum deviation from the dial gauge readings was 1.5 mil which is a factor of 3.5 better than the full field accuracy. This last demonstration indicates that proportional accuracy can be improved if suitable constraints are placed on the measurement.

6. CONCLUDING REMARKS

The accuracy of two solid-state array cameras and a commercially available PC controlled digital video image acquisition system for measuring wing deflection has been shown to be about 5 mil rms under best case conditions (no-flow) over a 26.5 inch semi-span test wing. The accuracy of the system for controlled single point deflection measurements is less than 2 mil. If sensors are not available in the model to provide accurate values of pitch and roll, then large bias errors are likely in spanwise deflection plots due to error in computing roll angle photogrammetrically with a limited number of inboard undeflected targets. The roll angle error does not affect the twist angle measurement which is mainly sensitive to pitch errors. Wing twist errors at the tip as large as 0.2° may be experienced with the present system, even after suitable least squares fits.

REFERENCES

1. Howell, R. R. The National Transonic Facility: Status and Operational Planning. AIAA-80-0415, AIAA 12th Aerodynamic Testing Conference, pp. 1-9 Mar. 1980.

2. Hertel, R. J. Stereo-Electro-Optical Tracker System for the Measurement of Model Deformation at the National Transonic Facility. NASA CR-159146, Oct. 1979.

3. Harding, K. and Harris, J. Evaluation of Moire Technique for Wind Tunnel Metrology. UDR-TR-81-111, University of Dayton Research Institute, Oct. 1981.

4. Hildebrand, B. P. and Doty, J. L. A Study of Model Deformation Measurement Techniques Applicable Within the National Transonic Facility. NASA CR-165853, Feb. 1982.

5. Brooks, J. D. and Beamish, J. K. Measurement of Model Aeroelastic Deformations in the Wind Tunnel at Transonic Speeds Using Stereo photogrammetry. NASA TP 1010, Oct. 1977.

6. Burner, A. W., Snow, W. L., Goad, W. K. Model Deformation Measurements at a Cryogenic Wind Tunnel Using Photogrammetry. Instrumentation in the Aerospace Industry, ISA vol. 31, pp.

615-622, May 1985.

7. Burner, A. W., Snow, W. L., Goad, W. K. Close-Range Photogrammetry with Video Cameras. 51st Annual Meeting ASP vol. 1, pp. 62-77, Mar. 1985.

8. Silicon Video User's Manual. ver 1.2, Epix, Inc., Oct. 1986.

9. Murty, M. V. R. K. The Use of a Single Plane Parallel Plate as a Lateral Shearing Interferometer with a Visible Gas Laser Source. Appl. Opt. vol. 3, no. 4, pp. 531-534, Apr. 1964.

10. Curry, S., Baumrind, S., Anderson, J. M. Calibration of an Array Camera. 51st Annual Meeting ASP vol. 1, pp. 331-340, Mar. 1985.

11. El-Hakim, S. F. Real-Time Image Metrology with CCD Cameras. Photo. Eng. & Remote Sens. vol. 52, no. 11, pp. 1757-1766, Nov. 1986.

12. Brown, D. C. Application of Close-Range Photogrammetry to Measurements of Structures in Orbit. vol. 1, Geodetic Services Inc. TP 80-012, 1980.

13. Smith, W. J. The Specification of Optical Shop Tolerances. Optical Spectra, pp. 19-21, Jan. 1967.